JACS
JOURNAL OF THE AMERICAN CHEMICAL SOCIETY
pubs.acs.org/JACS
Article

Mg-Ion Conduction in Antiperovskite Solid Electrolytes Revealed by ^{25}Mg Ultrahigh Field NMR and First-Principles Calculations

David M. Halat,*,☆ Haoyu Liu,☆ Kwangnam Kim, Grant C. B. Alexander, Xiaoling Wang, Amrit Venkatesh, Adam R. Altenhof, Harris E. Mason, Saul H. Lapidus, Jeong Seop Yoon, Ivan Hung, Zhehong Gan, Jordi Cabana, Donald J. Siegel,* Jeffrey A. Reimer,* and Baris Key*

Cite This: J. Am. Chem. Soc. 2025, 147, 27949−27961

Read Online

ACCESS | Metrics & More | Article Recommendations | Supporting Information

ABSTRACT: Magnesium-ion batteries hold the potential to outperform the energy density of lithium-ion batteries, given the divalent charge carried by each Mg^{2+} cation, but remain in an early stage of development. Here, ^{25}Mg solid-state nuclear magnetic resonance (ssNMR) is used to gain insight into the local structure and Mg-ion dynamics of candidate Mg-ion solid electrolytes, the antiperovskites Mg_3SbN and Mg_3AsN. Using the highest available magnetic field (35.2 T) for high-resolution solid-state NMR, the largest ^{25}Mg quadrupole coupling constants (C_Q) yet measured of up to 22 MHz are reported and corroborated by first-principles calculations. Predicted C_Q values are shown to correlate with the antiperovskite's tolerance factor; thus, ^{25}Mg NMR linewidths can report on lattice distortions and phase stability of these antiperovskites. Variable-temperature ^{25}Mg NMR spectra demonstrate changes at elevated temperatures, ascribed to Mg-ion motional effects. ^{25}Mg T_1 relaxometry measurements at ultrahigh field reveal a lower activation energy for the more distorted Mg_3AsN phase, matching computational predictions of a lower energy barrier for Mg^{2+} ion migration and suggesting that additional scrutiny of antiperovskites as Mg-ion conductors is warranted. Given the inherent challenges of ^{25}Mg NMR, this work demonstrates the benefits of combining ultrahigh field NMR spectroscopy, advanced pulse sequences, modern signal processing, and first-principles calculations to facilitate NMR of quadrupolar nuclei as a tool to probe the local structure and ion dynamics in beyond-Li battery materials.

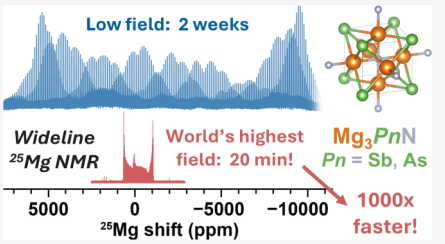

INTRODUCTION

Rechargeable batteries play a critical role in meeting the rapidly growing demand for large-scale energy storage.[1,2] Thanks to their high energy and power densities and their ability to withstand long-term cycling, Li-ion batteries are the current champions in the field. However, the performance of Li-ion systems is now beginning to plateau, and "beyond-Li" chemistries are of outstanding interest to enable continued advances in energy storage. Magnesium-ion batteries in particular are emerging as next-generation devices with the promise to surpass existing Li-ion systems, given the high theoretical capacities enabled by the divalent nature of Mg.[3−5] Mg is also more abundant than Li in the Earth's crust, translating to wider availability, lower cost, and reduced environmental impact.[6]

Recently, progress in the development of rechargeable Mg-ion batteries has resulted in improvements in both electrodes and electrolytes.[7−12] As a further improvement, the development of solid electrolytes would address potential safety concerns by replacing volatile and flammable liquid-based organic electrolytes.[11] More importantly, solid electrolytes are more compatible with metallic anodes, boosting both specific and volumetric capacities.[6,12] At a fundamental level, the rapid transport of multivalent species within solid networks remains a foundational challenge in solid-state ionics.

Among the possible solid electrolytes, antiperovskite frameworks are noteworthy because they accommodate a wide range of compositions and exhibit high ionic conductivities for some metal cations.[13−15] These materials adopt the formula X_3AB (X = cations, e.g., Li, Na, and Mg; A and B are anions).[16] Some Mg antiperovskites based on pnictogen anions (e.g., Pn = N, P, As, Sb, and Bi) have been experimentally synthesized, and additional Mg- and Ca-based compounds have been predicted via first-principles calculations to be stable.[17] In particular, two pnictogen-based antiperovskites, Mg_3AsN and Mg_3SbN, were predicted to exhibit promising stability with respect to Mg anodes and low energy barriers for percolating Mg-ion migration.[17] However, the Mg-ion transport processes in these systems remain to be confirmed experimentally. Moreover, unlike Li-, Na-, and K-based antiperovskites, which show a correlation between thermodynamic stability and the Goldschmidt structural tolerance factor,[18] such trends

Received: May 2, 2025
Revised: July 7, 2025
Accepted: July 10, 2025
Published: July 24, 2025

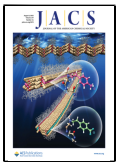

https://doi.org/10.1021/jacs.5c07442
J. Am. Chem. Soc. 2025, 147, 27949−27961

remain less certain for Mg-based analogues. Relatively few Mg-based antiperovskites have been synthesized, and those that have tend to exhibit high tolerance factors.[19−21] Further work is needed to assess the stability and ion transport properties of these materials.

A powerful experimental probe of cation transport in Mg-ion conductors is ^{25}Mg solid-state nuclear magnetic resonance (ssNMR); this method resolves the local structure of Mg^{2+} cations and can report on cation motion relevant to Mg-ion conductivity.[22,23] However, acquisition and interpretation of ^{25}Mg NMR spectra remain technically nontrivial. Due to its sparse natural abundance (10.0%) and low gyromagnetic ratio (γ = 2.606 MHz/T), the receptivity of ^{25}Mg is only 0.027% that of ^{1}H; this requires longer acquisition times to overcome instrumental artifacts and obtain adequate signal-to-noise ratios (SNR).

Moreover, ^{25}Mg is a quadrupolar, spin-5/2 nuclide with a large nuclear quadrupole moment (Q = 199.4 mbarn).[24] ^{25}Mg NMR spectra are strongly influenced by nuclear quadrupole interactions, presenting both challenges and opportunities. The asymmetrical charge distribution of the nucleus interacts with the local electric field gradient (EFG), if it is present. Thus, the nucleus can play the role of reporting on local charge and bonding asymmetry.[25−30] However, the local geometry of Mg-ion environments can also lead to overly broad spectra due to significant quadrupolar-induced linewidth broadening. This is exacerbated by the nature of the cation sites within cubic antiperovskites, which possess a very characteristic local environment, often giving rise to the largest known quadrupole coupling (C_Q) constants for their respective NMR-active nuclei.[31,32] In the materials under study, Mg_3AsN and Mg_3SbN, the local Mg environments are extremely asymmetric due to the octahedral coordination of Mg^{2+} cations with two N anions and four coplanar As or Sb anions (Figure 1). ^{25}Mg NMR should be an exquisitely sensitive probe of cation motion, yet the spectra are expected to be extremely challenging to acquire.

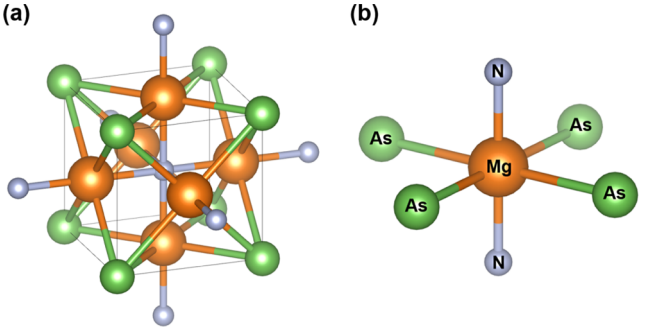

Figure 1. (a) Unit cell indicating the crystal structure of Mg_3AsN (cubic, *Pm*-3*m*) and (b) local Mg-ion environment, with two nitride and four arsenide neighbors, in a nominally octahedral configuration. Orange, green, and gray spheres indicate Mg, As, and N, respectively. Mg_3SbN adopts an analogous structure, with a slightly larger lattice parameter a = 4.354 Å (vs 4.220 Å for Mg_3AsN).

In order to improve the sensitivity of ^{25}Mg NMR, advanced pulse programs such as quadrupolar Carr−Purcell−Meiboom−Gill (CPMG) experiments have been introduced; these methods leverage long spin−spin (T_2') relaxation times of quadrupolar nuclei in solids.[33−35] CPMG sequences employ a standard $\pi/2$ pulse, followed by a series of spaced π pulses, to produce an echo train, greatly enhancing SNR for a given experimental time.[36,37] This sequence has been further optimized giving rise to the WURST-CPMG experiment, wherein $\pi/2$ and π pulses are replaced with wideband uniform-rate smooth truncation (WURST) pulses that provide broadband excitation and enable rapid acquisition of ultra-wideline spectra frequently encountered in ssNMR of quadrupolar nuclei.[38,39] The power of modern pulse sequences can be further unleashed by measurements at high magnetic field strength, as second-order quadrupolar broadening decreases proportionally with increasing magnetic field.[40] The 35.2 T Series-Connected Hybrid (SCH) magnet, providing the highest available field strength for high-resolution NMR at present, has provided a platform for enabling challenging experiments on quadrupolar nuclei.[41] The advantages of ultrahigh field using the SCH have been extensively demonstrated through acquisition of spectra of half-integer quadrupolar nuclei such as ^{11}B, ^{17}O, ^{25}Mg, ^{27}Al, ^{35}Cl, ^{43}Ca, ^{67}Zn, ^{71}Ga, and ^{139}La.[42−56]

This work employs the world's highest magnetic field for NMR to perform natural-abundance ^{25}Mg QCPMG NMR on the proposed antiperovskite Mg-ion conductors Mg_3AsN and Mg_3SbN. Measurements at 35.2 T enable the unprecedentedly rapid acquisition of natural-abundance ^{25}Mg ssNMR spectra in ∼20 min. The largest known ^{25}Mg quadrupolar coupling constants (C_Q values) of up to 22 MHz are observed and validated by first-principles calculations. The large quadrupolar interaction is shown to correlate with the antiperovskite's tolerance factor; thus, ^{25}Mg NMR linewidths can report on lattice distortions and phase stability of these materials. In the case of Mg_3AsN, this structural distortion coincides with a lower activation barrier for Mg-ion transport but also with reduced phase stability, as evidenced by impurity formation and degradation under ambient conditions, thus directly probing tolerance factor/stability correlations. Improvements in SNR at ultrahigh field enable sophisticated variable-temperature relaxometry and exchange spectroscopy (EXSY) experiments, assessing the relative energy barriers for Mg-ion migration in these materials and suggesting a lower activation energy for the more distorted Mg_3AsN phase, in agreement with computational predictions. The measured energy barriers are low enough to encourage further study of these materials, particularly given that few fast Mg-ion conductors exist. The present methodology enables the detection of Mg-ion motion in prospective antiperovskite electrolytes at the atomic-scale.

EXPERIMENTAL SECTION

Synthesis of Mg_3SbN and Mg_3AsN. The synthesis of Mg_3PnN (*Pn* = As, Sb) was performed following procedures from the prior literature.[19,57] Ensuring an inert atmosphere for all steps in the synthesis is essential to avoid the degradation of both the reactant nitride and the resulting antiperovskite nitride−pnictide phase.

In an argon-filled MBraun LabMaster glovebox, a 12.7 mL grinding jar was filled with 10 mmol of granular Mg_3N_2 (Sigma-Aldrich, 99.9%), 10 mmol of powdered *Pn* (As: Sigma-Aldrich, 99.9%; Sb: Sigma-Aldrich, 99.9%), and ten 5 mm zirconia grinding balls prior to clamping shut the jar. The contents were milled in a Retsch PM200 Planetary Ball Mill at 350 rpm for 18 h. Following milling, the contents of the grinding jar were transferred back into the argon-filled glovebox, and 250 mg of homogenized Mg_3N_2/*Pn* powder was loaded into a 6 mm diameter die press inside a heavy-duty Ziploc bag to preserve the atmosphere during pellet pressing. After removing this assembly from the glovebox, 2 tons of pressure was applied for 5−10 min to create densified pellets, followed by immediate return to an

https://doi.org/10.1021/jacs.5c07442
J. Am. Chem. Soc. 2025, 147, 27949−27961

inert atmosphere or vacuum. Milling and pressing steps were found to be essential for material synthesis, as the mechanism of antiperovskite formation occurs from the local decomposition of Mg_3N_2 in the presence of neutral *Pn* to generate N_2 gas and the desired Mg_3PnN phase.

Following pellet preparation, the individual pellets were transferred to individual 12.7 mm OD fused quartz tubes. To mitigate any reaction with the quartz, pellets were either wrapped in tantalum foil or the fused quartz tubes were carbon-coated by acetone combustion under a high-temperature torch flame. The maximum loading was found to be one pellet (~250 mg) per tube. Due to the nature of the decomposition reaction that formed N_2, our synthetic method can accommodate this limited scale of synthesis; scaling up induces tube failure at elevated temperature and internal pressure.

Pellets were sealed into the tubes under vacuum pressure (20 μbar) and then heated in a computer-controlled furnace to a minimum temperature of 800 °C for at least 12 h. The resultant products were either yellow (Mg_3AsN) or gray-black (Mg_3SbN). The sealed fused quartz ampules were transferred to an argon-filled glovebox and then opened to access the desired product in powder form. All materials were stored in the glovebox prior to characterization by powder X-ray diffraction using a Bruker D8 ADVANCE powder diffractometer with a Cu Kα X-ray tube (Figure S1). The products were observed to undergo degradation in humid air within several minutes (Mg_3AsN) to several hours (Mg_3SbN).

Synchrotron XRD. Samples were prepared by loading Kapton capillaries (0.9 mm diameter) with fine powder and sealing them with epoxy in a glovebox under an inert atmosphere. High-resolution synchrotron powder diffraction data were collected with a wavelength of 0.414 Å at beamline 11-BM-B, Advanced Photon Source (APS), Argonne National Laboratory. The scanning was conducted with a step size of $2\theta = 0.001°$, a scan speed of 0.01°/s, and a 12-element Si(111) crystal analyzer/detector.[58] Rietveld refinements were performed using TOPAS v6 and GSAS II software (Figure S2).[59]

Solid-State NMR Spectroscopy. ^{25}Mg QCPMG variable-offset cumulative spectroscopy (VOCS)[60] ssNMR measurements were performed at three different fields (11.7, 18.8, and 35.2 T) with ^{25}Mg Larmor frequencies of 30.6, 49.0, and 91.7 MHz, respectively.

Lower-field measurements employed an 11.7 T Bruker Ascend 500 magnet with a Bruker AVANCE III spectrometer and a Phoenix NMR 5 mm static HX probe with variable-temperature capabilities. A calibrated $\pi/2$ pulse length of 3 μs was used (nutation was performed on 5 M aqueous $MgCl_2$ and the pulse length was divided by 3, given $I = 5/2$), with a pulse delay of 1 s. The carrier frequency step size for VOCS was ~2000 ppm, with a QCPMG spikelet spacing of 107 ppm; nine subspectra were acquired. Each FID was processed by applying exponential line broadening to each individual echo in a symmetrical manner about the echo top, and then the subspectra were subjected to a window filtering procedure[60] before summing the subspectra, according to previous reports.[28] Measurements were acquired at room temperature and 373 K.

Room-temperature ^{25}Mg NMR measurements at 18.8 T were performed on an 18.8 T Oxford midbore magnet ("800 #1") equipped with a Bruker AVANCE III HD console and a 3.2 mm Low-E HXY NMR probe, operating under static conditions, which was designed and built at the National High Magnetic Field Laboratory (NHMFL). The VOCS frequency step size was ~1000 ppm, and the QCPMG spikelet spacing was 61.5 ppm; WURST pulses of 50 μs with a sweep width of 250 kHz were used to improve excitation bandwidth, and a pulse delay of 1 s was used.

^{25}Mg NMR experiments at 35.2 T were performed on the Series-Connected Hybrid (SCH) NMR magnet designed and built at the NHMFL.[41] The SCH NMR spectrometer was equipped with a Bruker AVANCE NEO console and a 3.2 mm HX MAS NMR probe operated under static (nonspinning) conditions; the probe was designed and built at the NHMFL.[41] The probe is equipped with a magnetic flux sensor and an external ^{7}Li lock sample located 9 mm below the sample to regulate the magnetic field strength. Measurements were performed at 238 K, 298 K, and 333 K; relaxation-optimized pulse delays of 8 s for Mg_3AsN and 20 s for Mg_3SbN were used.

Analysis of NMR Data. In addition to analysis using the Bruker TopSpin software, the ^{25}Mg CPMG data were processed using a method similar to that developed in the previously reported Compressed Sensing Multiplicative (CoSeM) routine.[61] All processing scripts were written in Python 3.1 using the numpy, scipy, and nmrglue packages.[62] The individual CPMG datasets were first divided into individual echoes, and the echoes were summed together. Small timing offsets of the echoes were noted in the low-field (11.7 T) dataset, and the echoes were shifted by subdwell timings (a shift of 1.1 $\mu s \times (n-1)$ where n is the echo number) using spline interpolation (Figure S3). The final shifted and summed echo was used for CoSeM processing (Figure S3d). For our implementation of CoSeM, a custom-written iterative soft thresholding with deletion (IST-D)[63] was used for the compressed sensing reconstruction. A series of 2000 datasets were generated from the summed FID, using a random subselection of only 10% to 20% of the initial data points. Each of these datasets was reconstructed to 1024 spectral points using a randomly selected number of IST-D iterations ranging from 5 to 20 iterations. Of the final 2000 reconstructed spectra, 30% of the spectra were selected using the $l1/l2$-norm criterion proposed in the original CoSeM publication[61] and summed to produce a final denoised spectrum, which is presented in magnitude mode. Due to the initial small number of points in the summed echo (278), the final reconstruction suffered from noise "spikes", where a single point had a substantially lower value than its neighboring points (Figure S4). To eliminate these spikes, 35 additional reconstructions of 2000 spectra each were generated, where the echo was truncated incrementally. This process distributed these spikes at different positions in the final reconstruction without affecting the true spectral intensity. The final reconstruction comprised the maximum or skyline projection of these 35 individual reconstructions. The final reconstructed spectrum showed a substantial improvement in signal-to-noise without distortion of the final lineshapes (Figure S5).

Ultrahigh field experimental data at 35.2 T were compared with simulated spectra to extract ^{25}Mg quadrupolar parameters, as well as to provide an estimate of the chemical shift (Section S3); simulations were performed with both the dmfit and QUEST software packages,[64,65] with the former using the high-field approximation and the latter providing an exact diagonalization of the Zeeman-quadrupolar Hamiltonian. Given the large C_Q values, the exact simulation of powder patterns using QUEST is preferable; however, at the ultrahigh field of 35.2 T, no significant differences were observed between the two sets of simulations using the same set of NMR parameters (Figures S6 and S7).

DFT Calculations. Calculations were performed with the Vienna *ab initio* simulation package (VASP).[66] Core–valence electron interactions were treated with the projector-augmented wave method.[67,68] The generalized gradient approximation in the formulation of Perdew–Burke–Ernzerhof was used for exchange and correlation.[69] The plane-wave cutoff energy was set to 800 eV. The energy criterion for convergence of the self-consistency loop was set to 10^{-8} eV. The atomic structures were adopted from the authors' prior study.[17] k-point sampling was performed with a Γ-centered 11 × 11 × 11 mesh for cubic antiperovskites (5 atoms), a Γ-centered 8 × 8 × 6 mesh for orthorhombic antiperovskites (20 atoms), and a Γ-centered 11 × 11 × 8 mesh for the impurity phase Mg_3Sb_2 (5 atoms, described below). Three approaches were explored for calculating ^{25}Mg isotropic chemical shifts from the predicted shielding values.[35,70,71] All yielded similar results, and the shielding–shift equation in ref 35 was ultimately adopted. To simulate the nuclear quadrupolar interaction in NMR spectroscopy, the electric field gradient (EFG) tensors were calculated using the method by Petrilli et al. as implemented in VASP.[72] The asymmetry parameter (η_Q) was calculated from the principal components of the symmetrized EFG tensor (V), where, by convention, $|V_{zz}| > |V_{xx}| > |V_{yy}|$ and $0 \leq \eta_Q \leq 1$:[73]

https://doi.org/10.1021/jacs.5c07442
J. Am. Chem. Soc. 2025, 147, 27949–27961

$$\eta_Q = \frac{|V_{xx} - V_{yy}|}{|V_{zz}|}$$

The quadrupolar coupling constants (C_Q) were calculated from the electron charge (e), nuclear electric quadrupole moment (Q; 199.4 and −44.4 mbarns for ^{25}Mg and ^{43}Ca, respectively),[24,74] and Planck's constant (h), as follows:[73]

$$C_Q = \frac{eQV_{zz}}{h}$$

Note that the value of the nuclear electric quadrupole moment of ^{43}Ca, −44.4 mbarns, has been recommended by Burgess et al. to improve agreement between experimental and calculated ^{43}Ca C_Q values.[75]

RESULTS AND DISCUSSION

Structure Determination. Room-temperature powder X-ray diffraction (XRD) patterns (Figure S1) confirmed that as-synthesized Mg_3AsN and Mg_3SbN adopt high-symmetry cubic phases. Both materials belong to space group $Pm\text{-}3m$, characteristic of the aristotype antiperovskite structure. High-resolution synchrotron XRD measurements and subsequent Rietveld analysis (Figure S2) confirmed the phase purity of the materials. Mg_3SbN was >99 wt % pure, whereas the Mg_3AsN sample contained a Mg_3As_2 impurity (6.9 wt %), likely reflecting the more facile degradation of the As-containing phase (see Experimental Section). Structural refinement of the synchrotron XRD patterns corroborates the expected anti-perovskite structure (Figure 1), wherein As or Sb anions reside within the corner-sharing Mg_6N octahedral network. The lattice parameter increases from that of Mg_3AsN (a = 4.220 Å) to that of Mg_3SbN (a = 4.354 Å). This result is expected, given the increase in ionic radii of the pnictides from As^{3-} to Sb^{3-}.[76] Refined lattice parameter values are in very good agreement with prior computational[17] and experimental reports.[19] A more detailed comparison of structural stability and Goldschmidt tolerance factors follows the presentation of the NMR results.

Groundwork ^{25}Mg ssNMR Spectroscopy. To establish the feasibility of ^{25}Mg NMR measurements, static QCPMG VOCS NMR of Mg_3AsN was acquired at a lower field of 11.7 T; at this modest field, the second-order quadrupolar interaction is expected to dominate the central transition (CT) line shape and lead to extensive broadening. As shown in Figure 2a, the ^{25}Mg spectrum at 11.7 T comprises an extremely broad quadrupolar powder pattern spanning 15000 ppm or nearly 500 kHz. Despite its breadth, the powder pattern corresponds to a nearly axially symmetric EFG tensor ($\eta_Q \approx 0$); this concurs with the symmetry of the local Mg^{2+} cation environment depicted in Figure 1, demonstrating the feasibility of local structure determination by ^{25}Mg NMR. However, due to the large number of frequency offsets required to span the full powder pattern, acquisition of the low-field spectrum took an extended period of ∼14 days. This duration limited the viability of more advanced experiments such as variable temperature measurements that would report on Mg-ion dynamics. We were motivated to perform acquisition at a higher field, where the expected increase in signal-to-noise ratio (SNR) would facilitate more rapid signal detection.

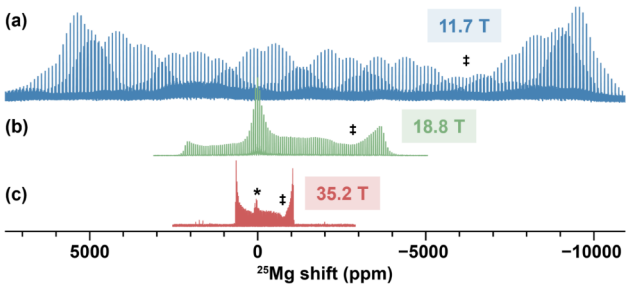

Figure 2. Variable-field ^{25}Mg solid-state NMR spectra of Mg_3AsN acquired at field strengths of (a) 11.7 T, (b) 18.8 T, and (c) 35.2 T. Acquisition times of 2 weeks, 2 days, and 20 min, respectively, were required. Recycle delays of 1 s were used at 11.7 and 18.8 T, while an optimized recycle delay of 8 s was used at 35.2 T. *Mg_3As_2 impurity. ‡Depletion of signal due to overlap of central transition (CT) and satellite transitions (ST).[78]

Figure 2 highlights the effect of magnetic field strength on acquisition. At a higher intermediate field strength of 18.8 T, we observe significant narrowing of the spectrum (Figure 2b), as expected from the field dependence of quadrupolar broadening. Despite halving the number of frequency offsets and achieving enhanced SNR per unit time at higher field, acquisition under these conditions entailed ∼2 days. We next conducted measurements at the SCH. At this ultrahigh field strength of 35.2 T, a significantly narrower static ^{25}Mg spectrum, ∼1700 ppm (160 kHz) wide (Figure 2c), was collected. The narrower width allowed acquisition within the excitation bandwidth corresponding to a single carrier frequency, eliminating the need for time-consuming VOCS measurements. Under these conditions, the ^{25}Mg QCPMG spectrum, characterized by a clearly defined, axially symmetric quadrupolar powder pattern, was captured in only 20 min; this reflects a thousand-fold time savings compared to acquisition at lower magnetic field.

In addition to enabling more advanced experiments, ^{25}Mg NMR at ultrahigh field provides further advantages, including simplified experimental optimization due to shorter measurement times. At the intermediate field (18.8 T), insufficient optimization of the recycle delay enhances the intensity of secondary signals near 0 ppm (Figure 2b). These signals are assigned to a minor Mg_3As_2 impurity phase, as supported by prior ^{25}Mg NMR literature on isostructural Mg_3Sb_2, which shows similar static ^{25}Mg shifts near 0 ppm,[77] and by our chemical shift calculations (see Table S1). Importantly, the relatively short relaxation time of this phase (∼0.1 s in prior work[77]) leads to signal overrepresentation when nonoptimized recycle delays are used. Measurements at the ultrahigh field of 35.2 T (Figure 2c) were instead optimized to be quantitative; the ∼0 ppm signal clearly observed at 18.8 T is therefore confidently assigned to the Mg_3As_2 impurity. At ultrahigh field, this secondary signal more accurately reflects the weight fraction as determined by diffraction (6.9 wt %).

Ultrahigh-field powder patterns lend themselves to examination of subtle spin interaction phenomena, such as the characteristic depletion of the signal at specific frequencies (indicated by ‡ in Figure 2). This "magic-angle hole" effect,[78] more prominent in axially symmetric systems, arises from the coherence transfer between the central transition (CT) and satellite transitions (ST) associated with the quadrupolar spin states due to energy level crossing.[79,80] At these specific overlap frequencies, radiofrequency excitation is no longer selective for the CT, resulting in concomitant "leakage" to the ST and a decrease of the intensity.[78] Although this behavior is present across all spectra in Figure 2, it is more readily apparent at ultrahigh field (Figure 2c).

https://doi.org/10.1021/jacs.5c07442
J. Am. Chem. Soc. 2025, 147, 27949−27961

Structural Comparison of Pnictogen Antiperovskites. Figure 3 shows ultrahigh field ^{25}Mg NMR that reveals clear differences between the Mg_3AsN and Mg_3SbN phases. The quadrupolar powder patterns of the two phases are primarily distinguished by linewidth; Mg_3AsN possesses the broader powder pattern. We fit experimental powder patterns to extract the ^{25}Mg quadrupolar coupling constants C_Q and asymmetry values η_Q, as well as approximate chemical shifts (Figures S6 and S7). The quadrupolar interaction is dominant, and chemical shift anisotropy (CSA) values do not contribute significantly to the experimental line shapes. Including CSA parameters has a negligible impact on the quality of the fit. Based on the visual comparison of powder pattern simulations in the SI, we estimate that CSA spans below ~300 ppm are unlikely to produce detectable changes in the spectral profile under our experimental conditions. This places an approximate experimental upper bound on the CSA, which is consistent with our computed CSA spans of <100 ppm. While such CSA effects are not resolvable at 35.2 T, field-dependent simulations (see Supporting Information) using the calculated NMR parameters indicate that the line shape would begin to resemble an axially symmetric CSA-dominated powder pattern above 280 T; this is not experimentally viable and emphasizes the dominance of the quadrupolar interaction in our experiments. Extracted parameters are reported in Table 1, together with the results of DFT calculations performed on geometry-optimized cubic structures.

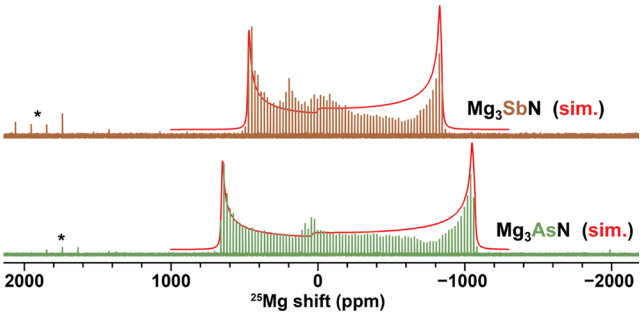

Figure 3. Comparison of ultrahigh field ^{25}Mg solid-state NMR spectra of Mg_3SbN (brown) and Mg_3AsN (green) acquired at ultrahigh field (35.2 T). Experimental spectra are overlaid with simulations (red) using the fitted quadrupolar parameters given in Table 1. Recycle delays of 8 s (Mg_3AsN) and 20 s (Mg_3SbN) were used. *High-frequency spikelet artifacts reflect interference from local FM broadcast radio signals close to the ^{25}Mg Larmor frequency (91.7 MHz).

As shown in Table 1, the DFT predictions agree remarkably well with the experimental NMR results. In particular, the experimental ^{25}Mg C_Q values of 19 and 22 MHz for Mg_3SbN and Mg_3AsN, respectively, with zero η_Q, showcase the well-defined, axially symmetric Mg-ion local environment depicted in Figure 1b. This local structure is a spectroscopic hallmark of the cubic antiperovskite phase. Excellent agreement between the experimental results and DFT calculations confirms that the quadrupolar NMR parameters of antiperovskites can be captured with high accuracy by computational methods. Previous studies of magnesium phosphates by Laurencin et al.[71] and Zhu and Huang[81] have generally found that ^{25}Mg C_Q values assessed by DFT significantly overestimate the experimental data; in this work, the good agreement between experiment and calculation may be due to the much simpler structural models of the antiperovskites or due to relatively slow Mg-ion motion that does not average the quadrupolar coupling, as described later.

Notably, we find that Mg_3AsN possesses the largest-known experimental ^{25}Mg C_Q of any known Mg-containing compound to date (22 MHz). The origin of the exceptional quadrupolar coupling constants in Mg antiperovskites can be rationalized using the method of Autschbach et al.[26] This method considers details of the electron density distribution due to specific bonds or ligands around the probe nucleus (here, ^{25}Mg). The C_Q is proportional to the largest component of the electric field gradient tensor, V_{zz}, and the orientation and magnitude of this component are often dictated by uneven electronic populations of orbitals that undergo bonding to the probe nucleus. It is readily apparent that symmetry arguments constrain the V_{zz} direction to lie along the Mg−N bond (see Figure 1b) but do not explain the origin of its large value. We attribute the large value of V_{zz} to a greater electronic density along the Mg−N bonds relative to the Mg−*Pn* bonds, which can be understood as a consequence of (1) the much shorter Mg−N bond distances (in Mg_3AsN, the Mg−N bond length is 2.12 Å, whereas the Mg−As bond length is 3.00 Å) and (2) the N p-states occupying lower-energy positions than the As (or Sb) p-states, as observed in prior calculations of the projected density of states of these antiperovskites.[19] The orientation of V_{zz} along the Mg−N bond is moreover confirmed by the present DFT calculations (see Section S4). Autschbach's method also allows us to rationalize the relative size of the C_Q values of 19 and 22 MHz for Mg_3SbN and Mg_3AsN, respectively. With smaller pnictide ionic radii (As^{3-} is smaller than Sb^{3-}), the decrease in the lattice parameter forces the contraction of all bonds, including the Mg−N bond, due to the structural constraints of the cubic antiperovskite structure. The Mg−N bond distance decreases from 2.19 Å (Mg_3SbN) to 2.12 Å (Mg_3AsN); this induces a concomitant increase in the electron density along this axis, increasing V_{zz} and thus also the ^{25}Mg C_Q in Mg_3AsN to an exceptional value of 22 MHz.

To our knowledge, the largest previously measured ^{25}Mg C_Q value is ~18 MHz, observed by Zhou et al. in the boracite-type compound $Mg_3B_7O_{13}Br$.[35] This compound possesses a local motif reminiscent of the antiperovskites in the present study,

Table 1. Comparison of ^{25}Mg NMR Parameters of Mg_3SbN and Mg_3AsN, Predicted from DFT Calculations and Extracted from Ultrahigh Field Solid-State NMR Measurements[a]

	DFT-predicted values				Experimental NMR data		
Compound	Shielding (ppm)	Chemical shift (ppm)	$\lvert C_Q \rvert$ (MHz)	η_Q	Chemical shift (ppm)	$\lvert C_Q \rvert$ (MHz)	η_Q
Mg_3SbN	550	15	18.4	0.0	0 ± 40	18.8 ± 0.2	~0
Mg_3AsN	554	10	22.1	0.0	40 ± 40	21.5 ± 0.2	~0

[a]Note that experimental data are insensitive to the sign of C_Q, so we compare its absolute value. The ^{25}Mg shielding-shift equation used for the calculated chemical shifts was $\delta_{iso} = -(\sigma_{iso} - 564.5 \text{ ppm})$.[35]

https://doi.org/10.1021/jacs.5c07442
J. Am. Chem. Soc. 2025, 147, 27949−27961

wherein Mg^{2+} ions reside in a nominally octahedral environment where the symmetry might naively be expected to result in a small C_Q value. However, as in the antiperovskite structure, bonding to two distinct anions, Br^- and O^{2-}, results in significant bond length variation. Thus, the local MgO_4Br_2 motif exhibits an elongated tetragonal dipyramid at the Mg site and a large ^{25}Mg C_Q value.[35] While the Mg−Br bond distance in $Mg_3B_7O_{13}Br$ of 2.02 Å is comparable to or even smaller than the Mg−N bonds in Mg_3AsN and Mg_3SbN, the C_Q values are larger in these antiperovskites. We attribute the larger C_Q values in the present work to the greater charge of N^{3-} as compared to Br^-, analogous to the situation observed in Na antiperovskites, wherein the ^{23}Na C_Q value of Na_3OCl, dictated by coordination to divalent O^{2-}, is larger than that of $Na_2NH_2BH_4$, in which Na^+ coordinates to monovalent NH_2^-.[31,82] While the present study reports the largest experimental ^{25}Mg quadrupolar coupling constants to date, we note that prior computational studies have predicted even larger C_Q values in organomagnesium compounds. In particular, Gervais et al. have reported calculated ^{25}Mg $|C_Q|$ values as large as 46 MHz in low-coordinate organometallic complexes.[83] These compounds often exhibit significant asymmetry in the electric field gradient ($\eta_Q \gg 0$) and multiple inequivalent Mg sites, suggesting that experimental spectra may be highly complex and overlapping; although these parameters remain to be verified experimentally by ^{25}Mg NMR, the use of ultrahigh field NMR and QCPMG techniques, as demonstrated here, may enable future measurements of such compounds. Nonetheless, our work establishes a new benchmark for experimentally measured ^{25}Mg C_Q values in inorganic solids.

For the generalized antiperovskite structure X_3AB, one can define the Goldschmidt tolerance factor[84] as

$$t = (R_X + R_B)/[\sqrt{2}(R_X + R_A)]$$

where R_X is the ionic radius of the cation, and R_A and R_B are the ionic radii of the anions. (In the following discussion, we compare analogous Mg and Ca antiperovskites; X = Mg^{2+} or Ca^{2+}.) The larger A-site anion resides within a corner-sharing octahedral framework comprising X-site cations and the smaller B-site anions. When t = 1, the ions optimally fill the space, resulting in a high-symmetry cubic structure ($Pm\text{-}3m$). A smaller tolerance factor (t < 1) implies a greater degree of distortion, eventually leading to the emergence of phases with lower-symmetry space groups.[18] Moreover, it has been shown that stability and ease of synthesizability are correlated with t; smaller tolerance factors imply a greater propensity for degradation and a narrower range of synthesis conditions.[85] Because the tolerance factor and C_Q values both reflect the degree of local distortion within the crystal structure, we hypothesize a correlation between these parameters: we expect that more distorted structures with small tolerance factors should translate into more asymmetric local environments, larger C_Q values, and broader quadrupolar powder patterns.

Figure 4 depicts the DFT-calculated ^{25}Mg and ^{43}Ca C_Q values for a range of multivalent pnictogen Mg and Ca antiperovskites, as a function of the tolerance factor, t. All compositions have been previously predicted to be stable,[17] and several have been successfully synthesized.[19,57,86] However, only the ^{25}Mg C_Q values of Mg_3AsN and Mg_3SbN have been confirmed experimentally in the present work. For the structures that adopt cubic phases (Mg_3AsN, Mg_3SbN, Mg_3BiN, Ca_3SbN, and Ca_3BiN), an inverse correlation is

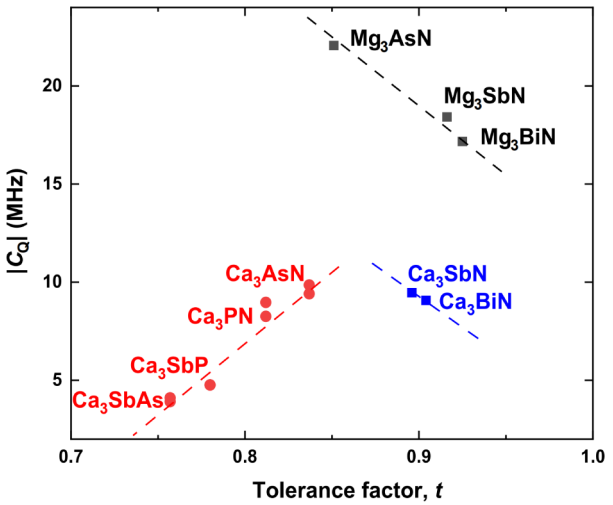

Figure 4. Correlation between tolerance factor and $^{25}Mg/^{43}Ca$ C_Q values for a range of pnictide antiperovskites: cubic Mg_3AsN, Mg_3SbN, and Mg_3BiN [black]; cubic Ca_3SbN and Ca_3BiN [blue]; and orthorhombic Ca_3SbAs, Ca_3SbP, Ca_3PN, and Ca_3AsN [red]. Data are given in Table S1. Two C_Q values are reported for each orthorhombic phase [red dots], reflecting the presence of two Ca sites in the lower-symmetry orthorhombic structure. (We compare absolute values of C_Q, as experiments are insensitive to its sign.)

observed, wherein C_Q increases as the tolerance factor decreases. This result confirms our hypothesis that less "ideal" cubic structures, with mismatched ionic radii, possess larger X-site C_Q values.

On the other hand, an opposite trend is observed for the more distorted Ca antiperovskites that adopt orthorhombic structures (t < 0.84). We attribute this decrease in ^{43}Ca C_Q to the loss of axial symmetry in the local cation environment within the lower-symmetry orthorhombic structure. While C_Q and η_Q are formally independent components of the electric field gradient (EFG) tensor, correlated variations between them can arise in real systems undergoing symmetry-lowering distortions. Czjzek explicitly demonstrated that statistical and geometric constraints in disordered environments can give rise to nontrivial correlations between V_{zz} and η_Q, despite the absence of direct mathematical dependence.[87] This behavior has also been observed experimentally: Butz reported that in the ferroelectric phase of $LiTaO_3$, the ^{181}Ta quadrupolar interaction exhibits a temperature-dependent decrease in V_{zz} and a corresponding increase in η, associated with symmetry-lowering structural distortions.[88] In our systems, larger distortions with smaller tolerance factors are reflected in decreases in the N−Mg−N bond angle (which is 180° in the ideal cubic phase). Given the prior discussion regarding the orientation of V_{zz} along the Mg−N bond, deviations away from axial symmetry should give rise to decreases in C_Q, as the computational results confirm. Local distortions associated with the orthorhombic phase are also reflected in increases in the η_Q parameter (see Table S1). However, C_Q and the tolerance factor alone cannot capture a universal structure−EFG trend across all compositions. To address this, we plot V_{zz} scaled by the relevant Sternheimer antishielding factor[89] against the cube of the Mg−B or Ca−B bond distance (generally B = N for most compounds in Figure 4); this axial bond aligns closely with the V_{zz} direction even in the lower-symmetry orthorhombic phases. The resulting plot reveals a monotonic trend across all compounds, suggesting that this

https://doi.org/10.1021/jacs.5c07442
J. Am. Chem. Soc. 2025, 147, 27949−27961

metric may serve as a robust universal descriptor of the structural influence on EFG tensors in antiperovskite phases (Supporting Information). Nonetheless, we anticipate that changes in quadrupolar parameters and the width of the corresponding experimental ^{25}Mg or ^{43}Ca NMR powder patterns will sensitively reflect changes in the thermodynamic stability of cubic antiperovskite phases. These considerations are also relevant in the context of orthorhombic−cubic phase transitions known to occur in Li and Na antiperovskites;[82,90] in these systems, spectral changes are correlated with the thermally activated onset of cation motion and overall ion conductivity. Our results confirm that ultrahigh field NMR can report directly on the stability of antiperovskites, providing a complement to traditional diffraction-based methods in evaluating phase stability and decomposition behavior.

Variable-Temperature ^{25}Mg NMR and Mg-Ion Dynamics. In addition to the structural information obtained by room-temperature ^{25}Mg NMR on stability and synthesizability, it is worth pondering if these antiperovskite phases could display features of solid-state electrolytes, namely thermally activated ionic conductivity, like their Li and Na counterparts. These features can be evaluated by variable-temperature (VT) NMR measurements. Temperature-dependent NMR line shapes can provide uniquely sensitive and quantitative insights into the mechanisms and dynamics of ion motion. For example, ^{23}Na VT-NMR measurements of $Na_2NH_2BH_4$ at and above room temperature have revealed Na^+ "hops" on the order of 10−100 kHz.[82] Lineshape-based VT-NMR methods can also probe phase transitions and their corresponding impacts on superionic transport, which are broadly useful for understanding the mechanism of ion transport in fast-ion conductors.[91−95]

We acquired variable-temperature ^{25}Mg NMR at ultrahigh field (35.2 T) between 238 and 333 K (Figure S8). Under these conditions, we observed relatively insignificant changes in line shapes, likely due to the limited accessible temperature range. Given these temperature constraints, we also acquired low-field data (at 11.7 T) at higher temperatures up to 430 K, focusing on the edges of the quadrupolar powder pattern to check for line shape narrowing that would provide direct evidence of cation motion. For Mg_3AsN, a comparison of spectra acquired at room temperature and 430 K, following postprocessing by the CoSeM denoising algorithm, does exhibit narrowing of the powder pattern (Figure S10). However, very minimal changes are observed; this suggests that Mg-ion motion is insufficiently rapid to significantly average the broad quadrupolar line shape, particularly given the large ^{25}Mg C_Q values. Moreover, the modest temperature-dependent narrowing observed for Mg_3SbN is in fact consistent with thermal expansion: using prior reports of thermal expansion coefficients,[96] an approximate calculation predicts a powder pattern contraction of ∼1.5% over this temperature range, corresponding to an inward shift of ∼10 ppm per edge (see Supporting Information), in agreement with the spectra (Figure S8c). Thus, no unambiguous signature of motional averaging is observed under these conditions, highlighting the need for complementary NMR measurements to assess the potential cation mobility. In contrast, prior ^{23}Na NMR data for antiperovskite $Na_2NH_2BH_4$ show characteristic spectral narrowing due to rapid sodium ion motion on the order of ∼100 kHz, admittedly with much smaller ^{23}Na quadrupolar coupling constants (5.5−6.8 MHz).[82] As discussed later, the low defect concentration in these Mg antiperovskites likely limits the Mg-ion hopping rates.

Given the limited changes in variable-temperature ^{25}Mg lineshapes, we suspected that other spectroscopic handles and advanced pulse sequences would be able to probe slower Mg-ion dynamics with greater sensitivity. NMR relaxometry, in particular, offers sensitivity to motional time scales complementary to those accessible via linewidth measurements.[97,98] We were able to perform ^{25}Mg T_1 (spin−lattice relaxation) measurements at ultrahigh field (35.2 T) thanks to the greatly enhanced SNR, where the acquisition time frame was mainly constrained by slow relaxation rates (∼0.1 Hz). We found that even at modest excursions from room temperature, the T_1 data are highly sensitive to temperature over the accessible range of 238−333 K (Figure 5). Fitting individual QCPMG spikelets

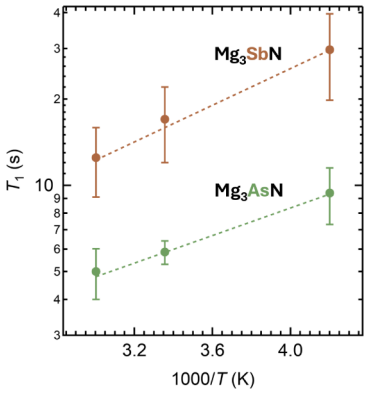

Figure 5. Variable-temperature ^{25}Mg spin−lattice relaxometry measurements of Mg_3SbN and Mg_3AsN acquired at ultrahigh field (35.2 T). Measurements were performed at 238 K, 298 K, and 333 K. Vertical bars indicate the distribution of spin−lattice relaxation constants arising from T_1 anisotropy. Dashed lines reflect Arrhenius-type fits to the data.

reveals a significant anisotropy in T_1 values across the quadrupolar powder patterns of both Mg_3AsN and Mg_3SbN (shown as vertical bars in Figure 5). In other words, the T_1 relaxation time depends on crystallite orientation and thus on isochromat frequency, i.e., spectral position within the second-order quadrupolar-broadened powder pattern. This anisotropy is quantitatively confirmed by relaxation-assisted separation[99] (RAS) analysis (Section S7). T_1 anisotropy has been previously reported for systems dominated by chemical shift anisotropy[100] and for ^{2}H NMR powder patterns,[101−103] and to our knowledge, there is at least one other example in prior literature in the case of second-order quadrupolar broadening of half-integer quadrupolar nuclei, specifically for ^{11}B MAS NMR of a catechol cyclic boronate ester at 9.4 T,[104] where comparable T_1 relaxation anisotropy to our case was observed, with a range of T_1 times from 16 to 22 s. (In the previous study by Altenhof et al., no discernible T_1 anisotropy was observed for quadrupolar-broadened ^{35}Cl NMR of glycine HCl.[101]) We credit the large T_1 anisotropy in this system to the exceptional ^{25}Mg C_Q values, demonstrating how highly quadrupolar-broadened spectra can strongly influence NMR relaxation mechanisms.

The VT-relaxometry data demonstrate that Mg_3SbN, as compared to Mg_3AsN, exhibits a greater dependence of the ^{25}Mg T_1 relaxation rate on temperature, as indicated by the steeper slope in Figure 5; this suggests a greater activation

https://doi.org/10.1021/jacs.5c07442
J. Am. Chem. Soc. 2025, 147, 27949−27961

barrier for Mg-ion motion in Mg_3SbN. The relaxometry data were quantitatively analyzed by the BPP theory (details in Section S8), under the assumption that relaxation rates were dominated by the quadrupolar mechanism; we believe that this assumption is reasonable, given the extraordinarily large C_Q values. Using the quadrupolar parameters previously extracted and confirmed by DFT calculations, relative activation energies were quantified using the Arrhenius equation (Figure S11).

The relaxometry data and BPP analysis reveal that the activation energy for Mg_3SbN is approximately 1.4 times larger than that in Mg_3AsN. Remarkably, this ratio is in quantitative agreement with previous nudged elastic band (NEB) calculations on these systems by Kim and Siegel.[17] The prior NEB simulations predict a limiting barrier ratio of either 1.3 (Mg_3SbN:Mg_3AsN), assuming a dumbbell mechanism for Mg-ion migration, or 1.5, assuming a vacancy-mediated mechanism). Both mechanisms are in quantitative agreement with our temperature-dependent relaxometry data. Activation energies derived from NMR data likely reflect local Mg-ion motion; as a rule, NMR does not probe long-range transport mechanisms, which in these materials are also improbable given the conceivably low defect concentration. The activation energy values derived from NMR in the present study (e.g., 45 meV in Mg_3AsN) are significantly smaller than those determined by NEB (e.g., 246 meV for dumbbell migration in Mg_3AsN; see Section S8); similar discrepancies have been reported in previous studies,[105,106] especially when comparing NMR with other techniques such as electrochemical impedance spectroscopy (EIS) measurements. This is commonly attributed to the sensitivity of NMR to local motional mechanisms, whereas larger E_a values obtained from measurements such as EIS reflect long-range processes and also grain boundary effects.[107,108] Despite this discrepancy, relative activation barriers are consistent across experimental and computational methods, quantitatively corroborating Mg-ion dynamics in Mg_3SbN and Mg_3AsN; moreover, the low activation energy values strengthen the case for further study of antiperovskites as potential solid-state Mg conductors.

Exchange spectroscopy (EXSY) NMR measurements can quantitatively probe the rate of exchange between NMR-distinct sites; typically, such measurements under our conditions would be extremely time-consuming, but rapid acquisition at ultrahigh field renders the technique feasible. Given time constraints, we performed a 1D EXSY rather than the conventional 2D version (Section S9). For Mg_3SbN, we observe clear evidence of Mg site exchange within the broad powder pattern, which demonstrates Mg-ion transport within crystallites and is observable in our system due to the three distinct orientations of the ^{25}Mg EFG tensor within the unit cell.[109] Our EXSY measurements quantitatively measure exchange rates on the order of seconds, suggesting Mg-ion hopping on the ~Hz time scale. This is significantly slower than ion transport previously observed in other systems such as Na antiperovskites,[82] which we attribute to the low concentration of defects (vacancies, interstitials) needed to mediate these hops.

Finally, we can relate the relative Mg-ion transport barriers to the antiperovskite structural attributes. The Goldschmidt tolerance factors provide a measure of the degree of structural distortion; smaller tolerance factors, indicating a greater degree of deviation from the ideal cubic structure ($t = 1$), have been correlated with a lower activation energy for Mg-ion migration.[17,110,111] Mg_3AsN, with a smaller activation barrier, also possesses a smaller tolerance factor ($t = 0.85$) as compared to Mg_3SbN ($t = 0.92$); a hypothesis explaining this trend is that the more distorted structure of Mg_3AsN generates a spectrum of energy barriers − some higher and some lower than the undistorted structure − and access to the lower barriers contributes to its enhanced Mg-ion motion. Further work is needed to establish whether the empirical correlation between tolerance factors and ion transport barriers holds in other antiperovskites and, moreover, what, if any, differences in behavior are seen in orthorhombic phases that exist below a critical value of the tolerance factor. We suggest that future antiperovskite syntheses geared to target high ionic conductivity may incorporate structural information about the expected tolerance factor, also with preliminary correlative NMR measurements, thereby informing design strategies for these solid-state electrolytes. We also note that phase stability may correlate with the tolerance factor in an adverse way. For example, in the present work, despite its lower barrier to Mg-ion migration, our Mg_3AsN sample notably contained a secondary Mg_3As_2 impurity (6.9 wt %) and experienced more facile degradation under ambient conditions. These challenges suggest a trade-off between optimization of ion conductivity and synthesizability and stability. Aliovalent doping strategies present a possible path forward, as doping could be employed to stabilize distorted or energetically unfavorable structures and increase the defect concentration, as has been reported in other Mg-ion solid electrolytes.[7,112,113] On the methodological side, given the large C_Q values observed in these systems, we note that nuclear quadrupolar resonance (NQR) spectroscopy presents an intriguing complementary approach for future characterization of antiperovskites; prior work has demonstrated the utility of $^{35/37}$Cl, $^{79/81}$Br, and ^{127}I NQR in similar high-C_Q systems, including perovskites with anion sites analogous to the local Mg^{2+} environments studied here.[114−117]

CONCLUSIONS

We employed the world's highest magnetic field for NMR to perform natural-abundance ^{25}Mg solid-state NMR on the antiperovskite prospective Mg-ion conductors Mg_3AsN and Mg_3SbN. Measurements at 35.2 T enabled rapid acquisition within 20 min of natural-abundance ^{25}Mg spectra, from which we confirmed the largest-known experimental ^{25}Mg quadrupolar coupling (C_Q) constants of up to 22 MHz, validated by DFT calculations. These large quadrupolar interactions provide insights into the local structure and phase stability. We demonstrate that Mg_3AsN, possessing the largest-known ^{25}Mg C_Q, exhibits the most distorted local Mg environment among all Mg-containing compounds studied by ^{25}Mg NMR. Variable-temperature ^{25}Mg NMR spectra reveal changes at elevated temperatures attributed to Mg-ion motional effects, with ^{25}Mg T_1 relaxometry measurements indicating a lower activation energy for the more distorted Mg_3AsN phase, consistent with prior computational predictions. Furthermore, exchange spectroscopy (EXSY) experiments quantitatively confirm Mg-ion hopping, highlighting slow (~Hz) motion in these materials. Given the outstanding problem of discovering fast Mg-ion conductors, the low activation energies measured in this work motivate additional study of these materials. The NMR measurements are consistent with empirical correlations between antiperovskite structural attributes such as Goldschmidt tolerance factors and ion transport barriers. We suggest that they can also provide insight into the relationships among stability, synthesizability, and ionic conductivity. The

https://doi.org/10.1021/jacs.5c07442
J. Am. Chem. Soc. 2025, 147, 27949−27961

present methodology demonstrates how a combination of ultrahigh field spectroscopy, advanced pulse sequences, modern signal processing, and DFT calculations can reveal local structure and ion dynamics in beyond-Li materials and paves the way for future design strategies aimed at optimizing the properties of promising antiperovskite solid-state electrolytes.

■ ASSOCIATED CONTENT

Supporting Information

The Supporting Information is available free of charge at https://pubs.acs.org/doi/10.1021/jacs.5c07442.

Powder diffraction patterns; DFT-predicted NMR parameters; spectral denoising and relaxation-assisted separation analysis; fitting and Arrhenius analysis of ultrahigh field spectra; additional ultrahigh field NMR measurements and simulations (PDF)

■ AUTHOR INFORMATION

Corresponding Authors

David M. Halat − *Department of Chemical and Biomolecular Engineering, University of California Berkeley, Berkeley, California 94720, United States; Department of Chemistry, Colorado School of Mines, Golden, Colorado 80401, United States; Materials Sciences Division, Lawrence Berkeley National Laboratory, Berkeley, CA 94720, United States;* orcid.org/0000-0002-0919-1689; Email: david.halat@mines.edu

Donald J. Siegel − *Walker Department of Mechanical Engineering, Texas Materials Institute, and Oden Institute for Computational Engineering & Sciences, The University of Texas at Austin, Austin, Texas 78712, United States;* orcid.org/0000-0001-7913-2513; Email: donald.siegel@austin.utexas.edu

Jeffrey A. Reimer − *Department of Chemical and Biomolecular Engineering, University of California Berkeley, Berkeley, California 94720, United States; Materials Sciences Division, Lawrence Berkeley National Laboratory, Berkeley, CA 94720, United States*; Email: reimer@berkeley.edu

Baris Key − *Chemical Sciences and Engineering Division, Argonne National Laboratory, Lemont, Illinois 60439, United States;* orcid.org/0000-0002-1987-1629; Email: bkey@anl.gov

Authors

Haoyu Liu − *Chemical Sciences and Engineering Division, Argonne National Laboratory, Lemont, Illinois 60439, United States;* orcid.org/0000-0002-6741-7295

Kwangnam Kim − *Mechanical Engineering Department, University of Michigan, Ann Arbor, Michigan 48109, United States; Laboratory for Energy Applications for the Future (LEAF), Lawrence Livermore National Laboratory, Livermore, California 94550, United States;* orcid.org/0000-0003-1149-1733

Grant C. B. Alexander − *Department of Chemistry, University of Illinois at Chicago, Chicago, Illinois 60607, United States*

Xiaoling Wang − *National High Magnetic Field Laboratory (NHMFL), Florida State University, Tallahassee, Florida 32310, United States; Department of Chemistry and Biochemistry, California State University East Bay, Hayward, California 94542, United States*

Amrit Venkatesh − *National High Magnetic Field Laboratory (NHMFL), Florida State University, Tallahassee, Florida 32310, United States;* orcid.org/0000-0001-5319-9269

Adam R. Altenhof − *MPA-Q, Los Alamos National Laboratory, Los Alamos, New Mexico 87545, United States*

Harris E. Mason − *Chemistry Division, Los Alamos National Laboratory, Los Alamos, New Mexico 87545, United States;* orcid.org/0000-0002-1840-0550

Saul H. Lapidus − *X-ray Science Division, Advanced Photon Source, Argonne National Laboratory, Lemont, Illinois 60439, United States;* orcid.org/0000-0002-7486-4325

Jeong Seop Yoon − *Walker Department of Mechanical Engineering, Texas Materials Institute, and Oden Institute for Computational Engineering & Sciences, The University of Texas at Austin, Austin, Texas 78712, United States;* orcid.org/0000-0002-9002-094X

Ivan Hung − *National High Magnetic Field Laboratory (NHMFL), Florida State University, Tallahassee, Florida 32310, United States;* orcid.org/0000-0001-8916-739X

Zhehong Gan − *National High Magnetic Field Laboratory (NHMFL), Florida State University, Tallahassee, Florida 32310, United States;* orcid.org/0000-0002-9855-5113

Jordi Cabana − *Department of Chemistry, University of Illinois at Chicago, Chicago, Illinois 60607, United States; Materials Science Division, Argonne National Laboratory, Lemont, Illinois 60439, United States;* orcid.org/0000-0002-2353-5986

Complete contact information is available at: https://pubs.acs.org/10.1021/jacs.5c07442

Author Contributions

☆D.M.H. and H.L. contributed equally to this manuscript. The manuscript was written through contributions of all authors; all authors have given approval to the final version of the manuscript.

Notes

The authors declare no competing financial interest.

■ ACKNOWLEDGMENTS

This work was intellectually led by the Joint Center for Energy Storage Research (JCESR), an Energy Innovation Hub funded by the U.S. Department of Energy (DOE), Office of Science, Basic Energy Sciences (BES), under Contract DE-AC02−06CH11357. Ultrahigh-field NMR experiments were performed at the 36 T Series-Connected Hybrid magnet at the National High Magnetic Field Laboratory, which is supported by National Science Foundation Cooperative Agreement No. DMR-2128556 and the State of Florida. Development of the 36 T Series-Connected Hybrid magnet and NMR instrumentation was supported by NSF (DMR-1039938 and DMR-0603042) and NIH (BTRR 1P41 GM122698). A part of the work by K. Kim was performed under the auspices of the U.S. Department of Energy by Lawrence Livermore National Laboratory (Contract No. DE-AC52-07NA27344). X.W. acknowledges the support of the U.S. Department of Energy (DOE) through grant DE-SC0025712. D.M.H. gratefully acknowledges support as a Pines Magnetic Resonance Center Postdoctoral Fellow. Dr. Michael A. Hope (University of Warwick) is gratefully acknowledged for helpful discussions and feedback. The authors acknowledge the Texas Advanced Computing Center (TACC) at The University of Texas at Austin for providing HPC resources that have contributed to

the research results reported within this article (URL: http://www.tacc.utexas.edu). This research used resources of the Advanced Photon Source, a U.S. Department of Energy (DOE) Office of Science user facility operated for the DOE Office of Science by Argonne National Laboratory under Contract No. DE-AC02-06CH11357. A portion of this work was carried out under the auspices of the U.S. Department of Energy by Los Alamos National Laboratory (Contract No. 89233218CNA000001).

REFERENCES

(1) Goodenough, J. B.; Park, K.-S. The Li-Ion Rechargeable Battery: A Perspective. *J. Am. Chem. Soc.* **2013**, *135*, 1167−1176.
(2) Liu, Y.; Zhu, Y.; Cui, Y. Challenges and Opportunities towards Fast-Charging Battery Materials. *Nat. Energy* **2019**, *4*, 540−550.
(3) Yoo, H. D.; Shterenberg, I.; Gofer, Y.; Gershinsky, G.; Pour, N.; Aurbach, D. Mg Rechargeable Batteries: An on-Going Challenge. *Energy Environ. Sci.* **2013**, *6*, 2265−2279.
(4) Liu, F.; Wang, T.; Liu, X.; Fan, L.-Z. Challenges and Recent Progress on Key Materials for Rechargeable Magnesium Batteries. *Adv. Energy Mater.* **2021**, *11*, 2000787.
(5) Canepa, P.; Sai Gautam, G.; Hannah, D. C.; Malik, R.; Liu, M.; Gallagher, K. G.; Persson, K. A.; Ceder, G. Odyssey of Multivalent Cathode Materials: Open Questions and Future Challenges. *Chem. Rev.* **2017**, *117*, 4287−4341.
(6) Muldoon, J.; Bucur, C. B.; Gregory, T. Quest for Nonaqueous Multivalent Secondary Batteries: Magnesium and Beyond. *Chem. Rev.* **2014**, *114*, 11683−11720.
(7) Jaschin, P. W.; Gao, Y.; Li, Y.; Bo, S.-H. A Materials Perspective on Magnesium-Ion-Based Solid-State Electrolytes. *J. Mater. Chem. A* **2020**, *8*, 2875−2897.
(8) Yoo, H. D.; Jokisaari, J. R.; Yu, Y.-S.; Kwon, B. J.; Hu, L.; Kim, S.; Han, S.-D.; Lopez, M.; Lapidus, S. H.; Nolis, G. M.; Ingram, B. J.; Bolotin, I.; Ahmed, S.; Klie, R. F.; Vaughey, J. T.; Fister, T. T.; Cabana, J. Intercalation of Magnesium into a Layered Vanadium Oxide with High Capacity. *ACS Energy Lett.* **2019**, *4*, 1528−1534.
(9) Kwon, B. J.; Yin, L.; Park, H.; Parajuli, P.; Kumar, K.; Kim, S.; Yang, M.; Murphy, M.; Zapol, P.; Liao, C.; Fister, T. T.; Klie, R. F.; Cabana, J.; Vaughey, J. T.; Lapidus, S. H.; Key, B. High Voltage Mg-Ion Battery Cathode via a Solid Solution Cr−Mn Spinel Oxide. *Chem. Mater.* **2020**, *32*, 6577−6587.
(10) Kwon, B. J.; Yin, L.; Roy, I.; Leon, N. J.; Kumar, K.; Kim, J. J.; Han, J.; Gim, J.; Liao, C.; Lapidus, S. H.; Cabana, J.; Key, B. Facile Electrochemical Mg-Ion Transport in a Defect-Free Spinel Oxide. *Chem. Mater.* **2022**, *34*, 3789−3797.
(11) Roth, E. P.; Orendorff, C. J. How Electrolytes Influence Battery Safety. *Electrochem. Soc. Interface* **2012**, *21*, 45.
(12) Hatzell, K. B.; Chen, X. C.; Cobb, C. L.; Dasgupta, N. P.; Dixit, M. B.; Marbella, L. E.; McDowell, M. T.; Mukherjee, P. P.; Verma, A.; Viswanathan, V.; Westover, A. S.; Zeier, W. G. Challenges in Lithium Metal Anodes for Solid-State Batteries. *ACS Energy Lett.* **2020**, *5*, 922−934.
(13) Li, Y.; Zhou, W.; Xin, S.; Li, S.; Zhu, J.; Lü, X.; Cui, Z.; Jia, Q.; Zhou, J.; Zhao, Y.; Goodenough, J. B. Fluorine-Doped Antiperovskite Electrolyte for All-Solid-State Lithium-Ion Batteries. *Angew. Chem., Int. Ed.* **2016**, *128*, 10119−10122.
(14) Dawson, J. A.; Attari, T. S.; Chen, H.; Emge, S. P.; Johnston, K. E.; Islam, M. S. Elucidating Lithium-Ion and Proton Dynamics in Anti-Perovskite Solid Electrolytes. *Energy Environ. Sci.* **2018**, *11*, 2993−3002.
(15) Dai, T.; Kouoi, X.; Reynaud, M.; Wagemaker, M.; Valldor, M.; Famprikis, T.; Koposov, A. Y. Antiperovskite Active Materials for Metal-Ion Batteries: Expected Advantages, Limitations, and Perspectives. *Energy Storage Mater.* **2024**, *68*, 103363.
(16) Dawson, J. A.; Famprikis, T.; Johnston, K. E. Anti-Perovskites for Solid-State Batteries: Recent Developments, Current Challenges and Future Prospects. *J. Mater. Chem. A* **2021**, *9*, 18746−18772.
(17) Kim, K.; Siegel, D. J. Multivalent Ion Transport in Anti-Perovskite Solid Electrolytes. *Chem. Mater.* **2021**, *33*, 2187−2197.
(18) Kim, K.; Siegel, D. J. Correlating Lattice Distortions, Ion Migration Barriers, and Stability in Solid Electrolytes. *J. Mater. Chem. A* **2019**, *7*, 3216−3227.
(19) Chi, E. O.; Kim, W. S.; Hur, N. H.; Jung, D. New Mg-Based Antiperovskites $PnNMg_3$ (*Pn* = As, Sb). *Solid State Commun.* **2002**, *121*, 309−312.
(20) Stoiber, D.; Niewa, R. Perovskite Distortion Inverted: Crystal Structures of $(A_3N)As$ (*A* = Mg, Ca, Sr, Ba). *Z. Für Anorg. Allg. Chem.* **2019**, *645*, 329−334.
(21) Heinselman, K. N.; Lany, S.; Perkins, J. D.; Talley, K. R.; Zakutayev, A. Thin Film Synthesis of Semiconductors in the Mg−Sb−N Materials System. *Chem. Mater.* **2019**, *31*, 8717−8724.
(22) Liu, Z.; Lee, J.; Xiang, G. J.; Glass, H. F. N.; Keyzer, E.; Dutton, S. P.; Grey, C. Insights into the Electrochemical Performances of Bi Anodes for Mg Ion Batteries Using ^{25}Mg Solid State NMR Spectroscopy. *Chem. Commun.* **2017**, *53*, 743−746.
(23) Bayliss, R. D.; Key, B.; Sai Gautam, G.; Canepa, P.; Kwon, B. J.; Lapidus, S. H.; Dogan, F.; Adil, A. A.; Lipton, A. S.; Baker, P. J.; Ceder, G.; Vaughey, J. T.; Cabana, J. Probing Mg Migration in Spinel Oxides. *Chem. Mater.* **2020**, *32*, 663−670.
(24) Pyykkö, P. Year-2008 Nuclear Quadrupole Moments. *Mol. Phys.* **2008**, *106*, 1965−1974.
(25) Kentgens, A. P. M. A Practical Guide to Solid-State NMR of Half-Integer Quadrupolar Nuclei with Some Applications to Disordered Systems. *Geoderma* **1997**, *80*, 271−306.
(26) Autschbach, J.; Zheng, S.; Schurko, R. W. Analysis of Electric Field Gradient Tensors at Quadrupolar Nuclei in Common Structural Motifs. *Concepts Magn. Reson. Part A* **2010**, *36A*, 84−126.
(27) van Bokhoven, J. A.; Koningsberger, D. C.; Kunkeler, P.; van Bekkum, H.; Kentgens, A. P. M. Stepwise Dealumination of Zeolite Beta at Specific T-Sites Observed with ^{27}Al MAS and ^{27}Al MQ MAS NMR. *J. Am. Chem. Soc.* **2000**, *122*, 12842−12847.
(28) Halat, D. M.; Britto, S.; Griffith, K. J.; Jónsson, E.; Grey, C. P. Natural Abundance Solid-State ^{33}S NMR Study of NbS_3: Applications for Battery Conversion Electrodes. *Chem. Commun.* **2019**, *55*, 12687−12690.
(29) Ashbrook, S. E.; Duer, M. J. Structural Information from Quadrupolar Nuclei in Solid State NMR. *Concepts Magn. Reson. Part A* **2006**, *28A*, 183−248.
(30) Ashbrook, S. E.; Sneddon, S. New Methods and Applications in Solid-State NMR Spectroscopy of Quadrupolar Nuclei. *J. Am. Chem. Soc.* **2014**, *136*, 15440−15456.
(31) Klösters, G.; Jansen, M. Determination of the (Na^+) Sternheimer Antishielding Factor by ^{23}Na NMR Spectroscopy on Sodium Oxide Chloride, Na_3OCl. *Solid State Nucl. Magn. Reson.* **2000**, *16*, 279−283.
(32) Darminto, B.; Rees, G. J.; Cattermull, J.; Hashi, K.; Diaz-Lopez, M.; Kuwata, N.; Turrell, S. J.; Milan, E.; Chart, Y.; Di Mino, C.; Jeong Lee, H.; Goodwin, A. L.; Pasta, M. On the Origin of the Non-Arrhenius Na-Ion Conductivity in Na_3OBr. *Angew. Chem., Int. Ed.* **2023**, *135*, No. e202314444.
(33) Jardón-Álvarez, D.; Bovee, M. O.; Baltisberger, J. H.; Grandinetti, P. J. Natural Abundance ^{17}O and ^{33}S Nuclear Magnetic Resonance Spectroscopy in Solids Achieved through Extended Coherence Lifetimes. *Phys. Rev. B* **2019**, *100*, 140103.
(34) de Oliveira, M.; Damasceno, H.; Salmon, P. S.; Eckert, H. Analysis and Information Content of Quadrupolar NMR in Glasses: ^{25}Mg NMR in Vitreous $MgSiO_3$ and $CaMgSi_2O_6$. *J. Magn. Reson. Open.* **2022**, *12*−*13*, 100067.
(35) Zhou, B.; Faucher, A.; Laskowski, R.; Terskikh, V. V.; Kroeker, S.; Sun, W.; Lin, J.; Mi, J.-X.; Michaelis, V. K.; Pan, Y. Ultrahigh-Field ^{25}Mg NMR and DFT Study of Magnesium Borate Minerals. *ACS Earth Space Chem.* **2017**, *1*, 299−309.
(36) Hung, I.; Rossini, A. J.; Schurko, R. W. Application of the Carr−Purcell Meiboom−Gill Pulse Sequence for the Acquisition of Solid-State NMR Spectra of Spin-1/2 Nuclei. *J. Phys. Chem. A* **2004**, *108*, 7112−7120.

https://doi.org/10.1021/jacs.5c07442
J. Am. Chem. Soc. 2025, 147, 27949−27961

(37) Hung, I.; Gan, Z. On the Practical Aspects of Recording Wideline QCPMG NMR Spectra. *J. Magn. Reson.* **2010**, *204*, 256−265.
(38) O'Dell, L. A.; Schurko, R. W. QCPMG Using Adiabatic Pulses for Faster Acquisition of Ultra-Wideline NMR Spectra. *Chem. Phys. Lett.* **2008**, *464*, 97−102.
(39) O'Dell, L. A.; Rossini, A. J.; Schurko, R. W. Acquisition of Ultra-Wideline NMR Spectra from Quadrupolar Nuclei by Frequency Stepped WURST−QCPMG. *Chem. Phys. Lett.* **2009**, *468*, 330−335.
(40) Vega, A. J. *Encyclopedia of Magnetic Resonance: Quadrupolar Nuclei in Solids*; Harris, R. K., Ed.; John Wiley & Sons, Ltd: Chichester, UK, 2007.
(41) Gan, Z.; Hung, I.; Wang, X.; Paulino, J.; Wu, G.; Litvak, I. M.; Gor'kov, P. L.; Brey, W. W.; Lendi, P.; Schiano, J. L.; Bird, M. D.; Dixon, I. R.; Toth, J.; Boebinger, G. S.; Cross, T. A. NMR Spectroscopy up to 35.2T Using a Series-Connected Hybrid Magnet. *J. Magn. Reson.* **2017**, *284*, 125−136.
(42) Dorn, R. W.; Heintz, P. M.; Hung, I.; Chen, K.; Oh, J.-S.; Kim, T.-H.; Zhou, L.; Gan, Z.; Huang, W.; Rossini, A. J. Atomic-Level Structure of Mesoporous Hexagonal Boron Nitride Determined by High-Resolution Solid-State Multinuclear Magnetic Resonance Spectroscopy and Density Functional Theory Calculations. *Chem. Mater.* **2022**, *34*, 1649−1665.
(43) Keeler, E. G.; Michaelis, V. K.; Colvin, M. T.; Hung, I.; Gor'kov, P. L.; Cross, T. A.; Gan, Z.; Griffin, R. G. ^{17}O MAS NMR Correlation Spectroscopy at High Magnetic Fields. *J. Am. Chem. Soc.* **2017**, *139*, 17953−17963.
(44) Martins, V.; Xu, J.; Hung, I.; Gan, Z.; Gervais, C.; Bonhomme, C.; Huang, Y. ^{17}O Solid-State NMR at Ultrahigh Magnetic Field of 35.2 T: Resolution of Inequivalent Oxygen Sites in Different Phases of MOF MIL-53(Al). *Magn. Reson. Chem.* **2021**, *59*, 940−950.
(45) Martins, V.; Xu, J.; Wang, X.; Chen, K.; Hung, I.; Gan, Z.; Gervais, C.; Bonhomme, C.; Jiang, S.; Zheng, A.; Lucier, B. E. G.; Huang, Y. Higher Magnetic Fields, Finer MOF Structural Information: ^{17}O Solid-State NMR at 35.2 T. *J. Am. Chem. Soc.* **2020**, *142*, 14877−14889.
(46) Wang, Q.; Li, W.; Hung, I.; Mentink-Vigier, F.; Wang, X.; Qi, G.; Wang, X.; Gan, Z.; Xu, J.; Deng, F. Mapping the Oxygen Structure of γ-Al_2O_3 by High-Field Solid-State NMR Spectroscopy. *Nat. Commun.* **2020**, *11*, 3620.
(47) Chen, C.-H.; Gaillard, E.; Mentink-Vigier, F.; Chen, K.; Gan, Z.; Gaveau, P.; Rebière, B.; Berthelot, R.; Florian, P.; Bonhomme, C.; Smith, M. E.; Métro, T.-X.; Alonso, B.; Laurencin, D. Direct ^{17}O Isotopic Labeling of Oxides Using Mechanochemistry. *Inorg. Chem.* **2020**, *59*, 13050−13066.
(48) Chen, K.; Horstmeier, S.; Nguyen, V. T.; Wang, B.; Crossley, S. P.; Pham, T.; Gan, Z.; Hung, I.; White, J. L. Structure and Catalytic Characterization of a Second Framework Al(IV) Site in Zeolite Catalysts Revealed by NMR at 35.2 T. *J. Am. Chem. Soc.* **2020**, *142*, 7514−7523.
(49) Shen, L.; Wang, Y.; Du, J.-H.; Chen, K.; Lin, Z.; Wen, Y.; Hung, I.; Gan, Z.; Peng, L. Probing Interactions of γ-Alumina with Water via Multinuclear Solid-State NMR Spectroscopy. *ChemCatChem* **2020**, *12*, 1569−1574.
(50) Madsen, R. S. K.; Qiao, A.; Sen, J.; Hung, I.; Chen, K.; Gan, Z.; Sen, S.; Yue, Y. Ultrahigh-Field ^{67}Zn NMR Reveals Short-Range Disorder in Zeolitic Imidazolate Framework Glasses. *Science* **2020**, *367*, 1473−1476.
(51) Shen, J.; Terskikh, V.; Wang, X.; Hung, I.; Gan, Z.; Wu, G. A Quadrupole-Central-Transition ^{17}O NMR Study of Nicotinamide: Experimental Evidence of Cross-Correlation between Second-Order Quadrupolar Interaction and Magnetic Shielding Anisotropy. *J. Phys. Chem. B* **2018**, *122*, 4813−4820.
(52) Bonhomme, C.; Wang, X.; Hung, I.; Gan, Z.; Gervais, C.; Sassoye, C.; Rimsza, J.; Du, J.; Smith, M. E.; Hanna, J. V.; Sarda, S.; Gras, P.; Combes, C.; Laurencin, D. Pushing the Limits of Sensitivity and Resolution for Natural Abundance ^{43}Ca NMR Using Ultra-High Magnetic Field (35.2 T). *Chem. Commun.* **2018**, *54*, 9591−9594.
(53) Zhang, W.; Hassan, A.; Struppe, J.; Monette, M.; Hung, I.; Gan, Z.; Martins, V.; Terskikh, V.; Huang, Y. Overcoming Challenges in ^{67}Zn NMR: A New Strategy of Signal Enhancement for MOF Characterization. *Chem. Commun.* **2023**, *59*, 5205−5208.
(54) Sen, S.; Stebbins, J. F.; Kroeker, S.; Hung, I.; Gan, Z. Evidence for Mixed Mg Coordination Environments in Silicate Glasses: Results from ^{25}Mg NMR Spectroscopy at 35.2 T. *J. Phys. Chem. B* **2023**, *127*, 10659−10666.
(55) Corti, L.; Hung, I.; Venkatesh, A.; Gor'kov, P. L.; Gan, Z.; Claridge, J. B.; Rosseinsky, M. J.; Blanc, F. Local Structure in Disordered Melilite Revealed by Ultrahigh Field ^{71}Ga and ^{139}La Solid-State Nuclear Magnetic Resonance Spectroscopy. *ChemPhysChem* **2024**, *25*, No. e202300934.
(56) Stirk, A. J.; Holmes, S. T.; Souza, F. E. S.; Hung, I.; Gan, Z.; Britten, J. F.; Rey, A. W.; Schurko, R. W. An Unusual Ionic Cocrystal of Ponatinib Hydrochloride: Characterization by Single-Crystal X-Ray Diffraction and Ultra-High Field NMR Spectroscopy. *CrystEngComm* **2024**, *26*, 1219.
(57) Chern, M. Y.; Vennos, D. A.; Disalvo, F. J. Synthesis, Structure, and Properties of Anti-Perovskite Nitrides Ca_3MN, M = P, As, Sb, Bi, Ge, Sn, and Pb. *J. Solid State Chem.* **1992**, *96*, 415−425.
(58) Lee, P. L.; Shu, D.; Ramanathan, M.; Preissner, C.; Wang, J.; Beno, M. A.; Von Dreele, R. B.; Ribaud, L.; Kurtz, C.; Antao, S. M.; Jiao, X.; Toby, B. H. A Twelve-Analyzer Detector System for High-Resolution Powder Diffraction. *J. Synchrotron Radiat.* **2008**, *15*, 427−432.
(59) Rietveld, H. M. A Profile Refinement Method for Nuclear and Magnetic Structures. *J. Appl. Crystallogr.* **1969**, *2*, 65−71.
(60) Tong, Y. Y. Nuclear Spin-Echo Fourier-Transform Mapping Spectroscopy for Broad NMR Lines in Solids. *J. Magn. Reson. A* **1996**, *119*, 22−28.
(61) Koprivica, D.; Martinho, R. P.; Novakovic, M.; Jaroszewicz, M. J.; Frydman, L. A Denoising Method for Multidimensional Magnetic Resonance Spectroscopy and Imaging Based on Compressed Sensing. *J. Magn. Reson.* **2022**, *338*, 107187.
(62) Helmus, J. J.; Jaroniec, C. P. Nmrglue: An Open Source Python Package for the Analysis of Multidimensional NMR Data. *J. Biomol. NMR* **2013**, *55*, 355−367.
(63) Shchukina, A.; Kasprzak, P.; Dass, R.; Nowakowski, M.; Kazimierczuk, K. Pitfalls in Compressed Sensing Reconstruction and How to Avoid Them. *J. Biomol. NMR* **2017**, *68*, 79−98.
(64) Massiot, D.; Fayon, F.; Capron, M.; King, I.; Le Calvé, S.; Alonso, B.; Durand, J.-O.; Bujoli, B.; Gan, Z.; Hoatson, G. Modelling One- and Two-Dimensional Solid-State NMR Spectra. *Magn. Reson. Chem.* **2002**, *40*, 70−76.
(65) Perras, F. A.; Widdifield, C. M.; Bryce, D. L. QUEST—QUadrupolar Exact SofTware: A Fast Graphical Program for the Exact Simulation of NMR and NQR Spectra for Quadrupolar Nuclei. *Solid State Nucl. Magn. Reson.* **2012**, *45*−*46*, 36−44.
(66) Kresse, G.; Furthmüller, J. Efficient Iterative Schemes for *Ab Initio* Total-Energy Calculations Using a Plane-Wave Basis Set. *Phys. Rev. B* **1996**, *54*, 11169−11186.
(67) Blöchl, P. E. Projector Augmented-Wave Method. *Phys. Rev. B* **1994**, *50*, 17953−17979.
(68) Kresse, G.; Joubert, D. From Ultrasoft Pseudopotentials to the Projector Augmented-Wave Method. *Phys. Rev. B* **1999**, *59*, 1758−1775.
(69) Perdew, J. P.; Burke, K.; Ernzerhof, M. Generalized Gradient Approximation Made Simple. *Phys. Rev. Lett.* **1996**, *77*, 3865−3868.
(70) Hu, J. Z.; Rajput, N. N.; Wan, C.; Shao, Y.; Deng, X.; Jaegers, N. R.; Hu, M.; Chen, Y.; Shin, Y.; Monk, J.; Chen, Z.; Qin, Z.; Mueller, K. T.; Liu, J.; Persson, K. A. ^{25}Mg NMR and Computational Modeling Studies of the Solvation Structures and Molecular Dynamics in Magnesium Based Liquid Electrolytes. *Nano Energy* **2018**, *46*, 436−446.
(71) Laurencin, D.; Gervais, C.; Stork, H.; Krämer, S.; Massiot, D.; Fayon, F. ^{25}Mg Solid-State NMR of Magnesium Phosphates: High Magnetic Field Experiments and Density Functional Theory Calculations. *J. Phys. Chem. C* **2012**, *116*, 19984−19995.

(72) Petrilli, H. M.; Blöchl, P. E.; Blaha, P.; Schwarz, K. Electric-Field-Gradient Calculations Using the Projector Augmented Wave Method. *Phys. Rev. B* **1998**, *57*, 14690−14697.
(73) Man, P. P. Quadrupole Couplings in Nuclear Magnetic Resonance, General. In *Encyclopedia of Analytical Chemistry*, Meyers, R. A.; John Wiley & Sons, Ltd: Chichester, UK, 2006; pp. 12224−12265. DOI: 10.1002/9780470027318.a611.
(74) Sahoo, B. K. Nuclear Quadrupole Moment of ^{43}Ca and Hyperfine-Structure Studies of Its Singly Charged Ion. *Phys. Rev. A* **2009**, *80*, 012515.
(75) Burgess, K. M. N.; Xu, Y.; Leclerc, M. C.; Bryce, D. L. Alkaline-Earth Metal Carboxylates Characterized by ^{43}Ca and ^{87}Sr Solid-State NMR: Impact of Metal-Amine Bonding. *Inorg. Chem.* **2014**, *53*, 552−561.
(76) Shannon, R. D. Revised Effective Ionic Radii and Systematic Studies of Interatomic Distances in Halides and Chalcogenides. *Acta Crystallogr., Sect. A* **1976**, *32*, 751−767.
(77) Murgia, F.; Laurencin, D.; Weldekidan, E. T.; Stievano, L.; Monconduit, L.; Doublet, M.-L.; Berthelot, R. Electrochemical Mg Alloying Properties along the $Sb_{1-x}Bi_x$ Solid Solution. *Electrochim. Acta* **2018**, *259*, 276−283.
(78) Hung, I.; Altenhof, A. R.; Schurko, R. W.; Bryce, D. L.; Han, O. H.; Gan, Z. Field-stepped Ultra-wideline NMR at up to 36 T: On the Inequivalence between Field and Frequency Stepping. *Magn. Reson. Chem.* **2021**, *59*, 951−960.
(79) Altenhof, A. R.; Lindquist, A. W.; Foster, L. D. D.; Holmes, S. T.; Schurko, R. W. On the Use of Frequen cy-Swept Pulses and Pulses Designed with Optimal Control Theory for the Acquisition of Ultra-Wideline NMR Spectra. *J. Magn. Reson.* **2019**, *309*, 106612.
(80) Kimball, J. J.; Altenhof, A. R.; Jaroszewicz, M. J.; Schurko, R. W. Broadband Cross-Polarization to Half-Integer Quadrupolar Nuclei: Wideline Static NMR Spectroscopy. *J. Phys. Chem. A* **2023**, *127*, 9621−9634.
(81) Zhu, J.; Huang, Y. A Natural Abundance Solid-State ^{25}Mg NMR Study of Layered Magnesium Phosphates. *Can. J. Chem.* **2011**, *89*, 803−813.
(82) Tsai, P.-C.; Mair, S.; Smith, J.; Halat, D. M.; Chien, P.-H.; Kim, K.; Zhang, D.; Li, Y.; Yin, L.; Liu, J.; Lapidus, S. H.; Reimer, J. A.; Balsara, N. P.; Siegel, D. J.; Chiang, Y.-M. Double Paddle-Wheel Enhanced Sodium Ion Conduction in an Antiperovskite Solid Electrolyte. *Adv. Energy Mater.* **2023**, *13*, 2203284.
(83) Gervais, C.; Jones, C.; Bonhomme, C.; Laurencin, D. Insight into the Local Environment of Magnesium and Calcium in Low-Coordination-Number Organo-Complexes Using ^{25}Mg and ^{43}Ca Solid-State NMR: A DFT Study. *Acta Crystallogr., Sect. C: Struct. Chem.* **2017**, *73*, 208−218.
(84) Goldschmidt, V. M. Die Gesetze der Krystallochemie. *Naturwissenschaften* **1926**, *14*, 477−485.
(85) Nagabhushana, G. P.; Shivaramaiah, R.; Navrotsky, A. Direct Calorimetric Verification of Thermodynamic Instability of Lead Halide Hybrid Perovskites. *Proc. Natl. Acad. Sci. U. S. A.* **2016**, *113*, 7717−7721.
(86) Amara, K.; Zemouli, M.; Elkeurti, M.; Belfedal, A.; Saadaoui, F. First-Principles Study of $XNMg_3$ (X = P, As, Sb and Bi) Antiperovskite Compounds. *J. Alloys Compd.* **2013**, *576*, 398−403.
(87) Czjzek, G. Distribution of Nuclear Quadrupole Splittings in Amorphous Materials and the Topology of the (V_{zz}, η)-Parameter Space. *Hyperfine Interact.* **1983**, *14*, 189−194.
(88) Butz, T. The Signature of the Nuclear Quadrupole Interaction in Continuous Phase Transitions. *Hyperfine Interact.* **1987**, *35*, 1037−1040.
(89) Schmidt, P. C.; Sen, K. D.; Das, T. P.; Weiss, A. Effect of Self-Consistency and Crystalline Potential in the Solid State on Nuclear Quadrupole Sternheimer Antishielding Factors in Closed-Shell Ions. *Phys. Rev. B* **1980**, *22*, 4167−4179.
(90) Wang, F.; Evans, H. A.; Kim, K.; Yin, L.; Li, Y.; Tsai, P.-C.; Liu, J.; Lapidus, S. H.; Brown, C. M.; Siegel, D. J.; Chiang, Y.-M. Dynamics of Hydroxyl Anions Promotes Lithium Ion Conduction in Antiperovskite Li_2OHCl. *Chem. Mater.* **2020**, *32*, 8481−8491.
(91) Duff, B. B.; Elliott, S. J.; Gamon, J.; Daniels, L. M.; Rosseinsky, M. J.; Blanc, F. Toward Understanding of the Li-Ion Migration Pathways in the Lithium Aluminum Sulfides Li_3AlS_3 and $Li_{4.3}AlS_{3.3}Cl_{0.7}$ via ^{6,7}Li Solid-State Nuclear Magnetic Resonance Spectroscopy. *Chem. Mater.* **2023**, *35*, 27−40.
(92) Hogrefe, K.; Stainer, F.; Minafra, N.; Zeier, W. G.; Wilkening, H. M. R. NMR Down to Cryogenic Temperatures: Accessing the Rate-Limiting Step of Li Transport in Argyrodite Electrolytes. *Chem. Mater.* **2024**, *36*, 6527−6534.
(93) Hempel, F. S.; Martineau-Corcos, C.; Bianchini, F.; Fjellvåg, H.; Arstad, B. Dynamics of Interlayer Na-Ions in Ga-Substituted $Na_2Zn_2TeO_6$ (NZTO) Studied by Variable-Temperature Solid-State ^{23}Na NMR Spectroscopy and DFT Modeling. *ACS Phys. Chem. Au.* **2023**, *3*, 394−405.
(94) Chen, Y.; Wang, P.; Truong, E.; Ogbolu, B.; Jin, Y.; Oyekunle, I.; Liu, H.; Islam, M. M.; Poudel, T.; Huang, C.; Hung, I.; Gan, Z.; Hu, Y.-Y. Superionic Conduction in K_3SbS_4 Enabled by Cl-Modified Anion Lattice. *Angew. Chem., Int. Ed.* **2024**, *63*, No. e202408574.
(95) Ashbrook, S. E.; Beran, G. J. O.; Blahut, J.; Blanc, F.; Brammer, L.; Brough, H.; Brown, S.; Bornes, C.; Charpentier, T.; Dracinsky, M.; et al. Challenges and Opportunities for NMR Calculations: General Discussion. *Faraday Discuss.* **2025**, *255*, 288−310.
(96) Belaroussi, T.; Amrani, B.; Benmessabih, T.; Iles, N.; Hamdache, F. Structural and Thermodynamic Properties of Antiperovskite $SbNMg_3$. *Comput. Mater. Sci.* **2008**, *43*, 938−942.
(97) Patel, S. V.; Banerjee, S.; Liu, H.; Wang, P.; Chien, P.-H.; Feng, X.; Liu, J.; Ong, S. P.; Hu, Y.-Y. Tunable Lithium-Ion Transport in Mixed-Halide Argyrodites $Li_{6-x}PS_{5-x}ClBr_x$: An Unusual Compositional Space. *Chem. Mater.* **2021**, *33*, 1435−1443.
(98) Kuhn, A.; Kunze, M.; Sreeraj, P.; Wiemhöfer, H.-D.; Thangadurai, V.; Wilkening, M.; Heitjans, P. NMR Relaxometry as a Versatile Tool to Study Li Ion Dynamics in Potential Battery Materials. *Solid State Nucl. Magn. Reson.* **2012**, *42*, 2−8.
(99) Altenhof, A. R.; Jaroszewicz, M. J.; Frydman, L.; Schurko, R. W. 3D Relaxation-Assisted Separation of Wideline Solid-State NMR Patterns for Achieving Site Resolution. *Phys. Chem. Chem. Phys.* **2022**, *24*, 22792−22805.
(100) Gibby, M. G.; Pines, A.; Waugh, J. S. Anisotropic Nuclear Spin Relaxation of ^{13}C in Solid Benzene. *Chem. Phys. Lett.* **1972**, *16*, 296−299.
(101) Altenhof, A. R.; Jaroszewicz, M. J.; Harris, K. J.; Schurko, R. W. Broadband Adiabatic Inversion Experiments for the Measurement of Longitudinal Relaxation Time Constants. *J. Chem. Phys.* **2021**, *154*, 034202.
(102) Wittebort, R. J.; Olejniczak, E. T.; Griffin, R. G. Analysis of Deuterium Nuclear Magnetic Resonance Line Shapes in Anisotropic Media. *J. Chem. Phys.* **1987**, *86*, 5411−5420.
(103) Long, J. R.; Ebelhäuser, R.; Griffin, R. G. ^{2}H NMR Line Shapes and Spin−Lattice Relaxation in $Ba(ClO_3)_2{\cdot}2H_2O$. *J. Phys. Chem. A* **1997**, *101*, 988−994.
(104) Oh, S.-W.; Weiss, J. W. E.; Kerneghan, P. A.; Korobkov, I.; Maly, K. E.; Bryce, D. L. Solid-State ^{11}B and ^{13}C NMR, IR, and X-Ray Crystallographic Characterization of Selected Arylboronic Acids and Their Catechol Cyclic Esters. *Magn. Reson. Chem.* **2012**, *50*, 388−401.
(105) Adediwura, S. C.; Mathew, N.; Günne, J. S. Combining NMR and Impedance Spectroscopy *in Situ* to Study the Dynamics of Solid Ion Conductors. *J. Mater. Chem. A* **2024**, *12*, 15847−15857.
(106) de Klerk, N. J. J.; van der Maas, E.; Wagemaker, M. Analysis of Diffusion in Solid-State Electrolytes through MD Simulations, Improvement of the Li-Ion Conductivity in β-Li_3PS_4 as an Example. *ACS Appl. Energy Mater.* **2018**, *1*, 3230−3242.
(107) Dunstan, M. T.; Griffin, J. M.; Blanc, F.; Leskes, M.; Grey, C. P. Ion Dynamics in Li_2CO_3 Studied by Solid-State NMR and First-Principles Calculations. *J. Phys. Chem. C* **2015**, *119*, 24255−24264.
(108) Ganapathy, S.; Yu, C.; Van Eck, E. R. H.; Wagemaker, M. Peeking across Grain Boundaries in a Solid-State Ionic Conductor. *ACS Energy Lett.* **2019**, *4*, 1092−1097.
(109) Southern, S. A.; Li, Y.; Liu, D.-J.; Sadow, A. D.; Qi, L.; Perras, F. A. Enhanced Activity from Coordinatively Unsaturated and

Dynamic Zeolite-Bound Organoscandium Species. *ACS Catal.* **2024**, *14*, 9440−9451.
(110) Kim, K.; Li, Y.; Tsai, P.-C.; Wang, F.; Son, S.-B.; Chiang, Y.-M.; Siegel, D. J. Exploring the Synthesis of Alkali Metal Anti-Perovskites. *Chem. Mater.* **2022**, *34*, 947−958.
(111) Kim, K.; Siegel, D. J. Machine Learning Reveals Factors That Control Ion Mobility in Anti-Perovskite Solid Electrolytes. *J. Mater. Chem. A* **2022**, *10*, 15169−15182.
(112) Halim, Z. A.; Adnan, S. B. R. S.; Salleh, F. M.; Mohamed, N. S. Effects of Mg^{2+} Interstitial Ion on the Properties of $Mg_{0.5+x/2}Si_{2-x}Al_x(PO_4)_3$ Ceramic Electrolytes. *J. Magnes. Alloys.* **2017**, *5*, 439−447.
(113) Wang, L.-P.; Zhao-Karger, Z.; Klein, F.; Chable, J.; Braun, T.; Schür, A. R.; Wang, C.-R.; Guo, Y.-G.; Fichtner, M. $MgSc_2Se_4$—A Magnesium Solid Ionic Conductor for All-Solid-State Mg Batteries? *ChemSusChem* **2019**, *12*, 2286−2293.
(114) Szell, P. M. J.; Bryce, D. L. Solid-State Nuclear Magnetic Resonance and Nuclear Quadrupole Resonance as Complementary Tools to Study Quadrupolar Nuclei in Solids. *Concepts Magn. Reson. Part A* **2016**, *45A*, No. e21412.
(115) Hooper, R. W.; Lin, K.; Veinot, J. G. C.; Michaelis, V. K. 3D to 0D Cesium Lead Bromide: A $^{79/81}$Br NMR, NQR and Theoretical Investigation. *J. Magn. Reson.* **2023**, *352*, 107472.
(116) Quarti, C.; Gautier, R.; Zacharias, M.; Gansmuller, A.; Katan, C. Nuclear Quadrupolar Resonance Structural Characterization of Halide Perovskites and Perovskitoids: A Roadmap from Electronic Structure Calculations for Lead−Iodide-Based Compounds. *J. Am. Chem. Soc.* **2025**, *147*, 278−291.
(117) Nari, A.; Rahman, M.; Szell, P. M. J.; Semeniuchenko, V.; Bryce, D. L. Halogen Bond Strength in Solids Quantified via Zeeman-Perturbed Nuclear Quadrupole Resonance Spectroscopy. *J. Am. Chem. Soc.* **2025**, *147*, 9528−9543.

https://doi.org/10.1021/jacs.5c07442
J. Am. Chem. Soc. 2025, 147, 27949−27961